3D displacement field of the 2015 M$_w$8.3 Illapel earthquake (Chile) from across- and along-track Sentinel-1 TOPS interferometry

R. Grandin[1], E. Klein[2], M. Métois[3], and C. Vigny[2]

Abstract

Wide-swath imaging has become a standard acquisition mode for radar missions aiming at applying SAR interferometry at global scale with enhanced revisit frequency. Increased swath width, compared to classical Stripmap imaging mode, is achieved at the expense of azimuthal resolution. This makes along-track displacements, and subsequently north-south displacements, difficult to measure using conventional split-beam (multiple-aperture) InSAR or cross-correlation techniques. Alternatively, we show here that the along-track component of ground motion can be deduced from the double-difference between backward- and forward-looking interferograms within regions of burst overlap. "Burst overlap interferometry" takes advantage of the large squint angle diversity of Sentinel-1 ($\sim 1°$) to achieve sub-decimetric accuracy on the along-track component of ground motion. We demonstrate the efficiency of this method using Sentinel-1 data covering the 2015 M$_w$8.3 Illapel earthquake (Chile) for which we retrieve the full 3D displacement field and validate it against observations from a dense network of GPS sensors.

1. Introduction

Since the pioneering contributions of the 1990s, monitoring of large-scale ground motion using Interferometric Synthetic Aperture Radar (InSAR) has made spectacular progress. Thanks to improvement of the phased array technology, advances in orbitography, increasing computational power as well as the launch of multiple civilian SAR missions since the 2000s, a broad range of natural and anthropogenic processes can be routinely monitored today [see *Simons and Rosen*, 2007, for a recent review]. Among these processes, the InSAR technique has proved extremely valuable in mapping the displacement

[1]Institut de Physique du Globe de Paris, Sorbonne Paris Cité, Université Paris Diderot, UMR 7154 CNRS, Paris, France.

[2]Laboratoire de Géologie, École Normale Supérieure, UMR 8538 CNRS, Paris, France.

[3]Laboratoire de Géologie de Lyon: Terre, Planètes, Environnement (LGLTPE), École Normale Supérieure de Lyon, Université Claude Bernard, UMR 5276 CNRS, Lyon, France.

field induced by large plate-boundary events, such as earthquakes or magmatic intrusions, especially in geographical areas where GPS measurements are lacking [e.g. *Peltzer et al.*, 1999; *Grandin et al.*, 2009].

One limitation of InSAR is that only the component of deformation in the sensor line-of-sight (LOS), i.e. the across-track component, can be resolved. Acquisitions from ascending and descending passes are usually combined to provide two different viewing geometries. Even so, due to the near-polar orbit of SAR satellites, resolution on the north-south component remains poor [*Wright et al.*, 2004].

Therefore, in complement to conventional InSAR, a number of signal processing techniques have been proposed to retrieve the horizontal component of displacement parallel to the satellite track. These methods, which rely either on the amplitude (incoherent cross-correlation, also termed offset tracking [*Michel et al.*, 1999; *Fialko et al.*, 2001]) or on the phase (multiple-aperture InSAR, also termed split-beam interferometry [*Bechor and Zebker*, 2006; *Barbot et al.*, 2008; *Jung et al.*, 2009]), typically allow for resolving displacements exceeding $\sim 10\%$ of the azimuth pixel size. Hence, for classical Stripmap mode (azimuth pixel size of the order of a few meters), displacements greater than a few decimeters can be resolved. As a consequence, the resolution that can be achieved with such methods restricts their applicability to the study of intermediate to large earthquakes ($M_w > 6$).

Recent advances in SAR technology and processing have allowed for the emergence of a new generation of sensors entirely dedicated to wide-swath imaging. Wide-swath modes allow for global mapping with an increased revisit frequency, as exemplified by the two satellites Sentinel-1 and ALOS-2, respectively operating TOPS and ScanSAR as standard acquisition modes. Unfortunately, the increase of the swath breadth by a factor 3 to 5 comes at the expense of reduced azimuthal resolution by an equivalent factor. Trading azimuth resolution for increased swath width, hence shortened revisit interval, is arguably advantageous for studying large-scale tectonic deformation, whether coseismic, postseismic or interseismic [e.g. *Grandin et al.*, 2015]. On the other hand, split-beam and offset-tracking techniques become limited to sensing along-track displacement exceeding ~ 50 cm, hence restricting their potential usefulness [*Jung et al.*, 2014].

Alternatively, we propose here to take advantage of wide-swath burst-modes, especially TOPS, by applying along-track interferometry in regions where successive bursts overlap in the azimuth direction (Figure 1). This technique, whose original objective was to improve the coregistration of a slave image against its master [*Scheiber and Moreira*, 2000; *Prats-Iraola et al.*, 2012], is used here for another purpose. We show that burst-overlap interferometry allows for resolving subtle motion along the azimuth direction. The technique is particularly efficient for Sentinel-1 TOPS data, as beam steering in azimuth provides an increased squint angle diversity within burst overlaps, hence a better resolution on horizontal motion compared to split-beam interferometry applied to Stripmap or ScanSAR images.

In this paper, focusing on the case study of the Illapel earthquake (Chile, 16 September 2015, $M_w 8.3$), we use Sentinel-1 wide-swath data to retrieve the full 3D surface displacement field. Independent measurements acquired by a continuous GPS network allow for validating the method and estimating its uncertainty.

2. Method

2.1. TOPS along-track interferometry

Sentinel-1 is the first SAR mission to implement the TOPS mode as a standard acquisition mode for interferometry (Figure 1) [*Torres et al.*, 2012]. Similar to ScanSAR, an extended swath is achieved in TOPS mode by electronically steering the beam in elevation periodicly so as to cover several adjacent sub-swaths (three in the case of Sentinel-1 "Interferometric Wide-swath" mode, IW) [*De Zan and Guarnieri*, 2006]. Each sub-swath is imaged in a succession of bursts, typically consisting of a thousand pulses. Because a given ground pixel is only illuminated during a fraction of the standard Stripmap-mode synthetic aperture duration, the resulting azimuth bandwidth of burst-modes, hence the achievable azimuth resolution, is decreased accordingly. On the other hand, the range properties of the images (bandwidth and resolution) are unchanged.

In ScanSAR mode, the beam angle with respect to zero-Doppler direction (also termed "squint" angle) is held fixed. In TOPS mode, a steady drift of the squint angle, from backward to forward, is introduced over the course of the burst transmission in order to broaden the size of the illuminated area in the azimuth direction (Figure 1a). As a result, TOPS achieves improved image quality both in terms of phase (reduced azimuth ambiguity) and amplitude (decreased "scalloping" effect) [*Meta et al.*, 2008]. Nevertheless, both ScanSAR and TOPS require accurate burst synchronization to warrant sufficient azimuth spectral overlap for interferometry [*Holzner and Bamler*, 2002].

In wide-swath mode, a small overlap region occurs between the bursts to ensure that the final processed image will be devoid of any gap (Figure 1a). In these "burst overlap regions", ground pixels are observed twice from two slightly different angles, or equivalently with two different Doppler centroid frequencies (Figure 1b). In ScanSAR mode, this azimuth angular separation is limited by beam aperture, which usually does not exceed 0.25°. In TOPS mode, the Doppler centroid difference is much greater, as a direct consequence of the squinted view introduced by beam steering in azimuth. For Sentinel-1, the difference in squint angle is typically of the order of 1°, with overlap regions corresponding to $\sim$ 10% of the burst length.

When processing TOPS data for interferometry, it is possible to take advantage of the slight difference in squint angles within overlap regions in order to retrieve the horizontal component of ground motion parallel to the satellite track. Akin to Multiple Aperture InSAR (MAI), a double difference of the phase within overlap regions is computed as follows (Figure 1b) : (1) calculate the interferogram using only the phase deduced from the forward view $\Delta\Phi_{\mathrm{fw}}$, (2) calculate the interferogram in the backward view $\Delta\Phi_{\mathrm{bw}}$, (3) compute the difference between forward-looking and backward-looking interferograms $\Delta\Phi_{\mathrm{ovl}} = \Delta\Phi_{\mathrm{fw}} - \Delta\Phi_{\mathrm{bw}}$ (see Appendix A for details). This technique will be thereafter refered to as "burst-overlap interferometry".

The final double-difference interferogram corresponds to the temporal variation of the difference in slant range from two slightly different squint angles. In observation scenarios devoid of any ground motion, the double-difference phase $\Delta\Phi_{\mathrm{ovl}}$ only includes the effect of slight errors in coregistration between the master and slave images [*Scheiber and Moreira*, 2000]. Hence, this procedure is commonly used to refine coregistration during TOPS InSAR processing, a method known as "enhanced spectral diversity" (ESD) [e.g. *Prats-Iraola et al.*, 2012]. On the other hand, when significant ground motion has occurred between two acquisitions, phase jumps across burst boundaries in TOPS interferograms are diagnostic of horizontal ground motion along the satellite track [e.g. *De Zan et al.*, 2014; *González et al.*, 2015]. The double-difference procedure allows for directly measuring this phase difference on a pixelwise basis within overlap regions. Topographic and tropospheric contributions are largely cancelled by the double-difference, which results in better phase quality than in the across-track interferogram.

2.2. Data set

In order to map the 3D displacement field of the 2015 $M_w 8.3$ Illapel earthquake, we use SAR data acquired by Sentinel-1A in IW TOPS mode. Images before the earthquake were acquired on 08/24/2015 and 08/26/2015 for the descending and ascending passes, respectively. Post-earthquakes acquisitions were performed on 09/17/2015 (+11 hours after quake) and 09/19/2015 (+3 days). Interferograms are computed using the method of *Grandin* [2015], starting from Level 1 Single Look Complex (SLC) products distributed by ESA. Precise orbits (https://qc.sentinel1.eo.esa.int) and SRTM 1-arcsecond DEM are used for orbital and topographic corrections. Azimuth phase deramping is calculated using precise coregistration derived from pixel offsets, and further refined by means of ESD within burst overlaps [*Prats-Iraola et al.*, 2012; *Grandin*, 2015]. Interferograms are multilooked by a factor 12 in range and 4 in azimuth, resulting in a ground pixel of ~ 60 m. Unwrapping is performed using the cut-tree algorithm [*Goldstein et al.*, 1988] and corrected manually when necessary.

Azimuth displacements are retrieved using the burst overlap interferometry technique (see Appendix A for details). Flat-Earth, topographic correction and multilooking are applied to the forward and backward interferograms prior to computation of the double-difference interferogram [*De Zan et al.*, 2015]. A spatial coherence mask with a threshold of 0.4 is applied to discard unreliable phase values. Pixels are low-pass filtered using 1 km-wide maximum likelihood estimator. Flattening of interferograms is performed by fitting a bilinear polynomial surface on the difference between, on one hand, GPS measurements from a local geodetic network [*Ruiz et al.*, 2016] projected onto the appropriate unit vector (along- or across-track) and, on the other hand, the nearest pixel in the interferogram. Finally, interpolation by a Laplacian operator is applied in order to fill the gaps between the bursts.

3. Results and discussion

3.1. Along-track InSAR

Across-track interferograms show a maximum line-of-sight displacement of $\pm$150 cm, picturing the semi-circular fringe pattern typical of subduction earthquakes in Chile [e.g. *Pritchard et al.*, 2006] (Figure 2, top). Displacement occurs exclusively away from the satellite in the descending pass and toward the satellite in the ascending pass. This is consistent with seaward motion reaching $\gtrsim 1$ m in the coastal area combined with moderate vertical displacement (within the range $\pm$50 cm) due to the offshore earthquake location. Furthermore, we notice that peak displacement in the descending across-track interferogram occurs $\sim$ 30 km to the north of the peak in the ascending interferogram. This suggests that displacement vectors experience substantial rotation, either about a vertical or horizontal axis, at 31°S. However, as a result of the acquisition geometry of InSAR, the vertical and north-south components cannot be distinguished in the across-track interferograms. Hence, all the details of the actual ground displacement field cannot be restituted solely from these two across-track interferograms.

In contrast, along-track interferograms show a more complex displacement pattern with both negative and positive displacements peaking at ±40 cm (Figure 2, bottom). Displacements vary smoothly over distances exceeding ∼ 20 km, which is twice the distance separating two consecutive burst overlap regions. This demonstrates that interpolation between burst overlaps did not lead to significant aliasing of the displacement field. Due to the near-polar orbit, along-track interferograms are strongly sensitive to the north-south component of motion, whereas across-track interferograms are least sensitive to this component. In the particular case of the Illapel earthquake, horizontal displacement occurs mostly trench-normal, i.e. with an azimuth of N260°. The ascending along-track interferogram, which is nearly insensitive to the trench-normal displacement, shows a sign reversal consistent with trench-parallel, southward motion in the north, shifting to trench-parallel, northward motion in the south. In the along-track descending interferogram, peak displacement occurs in the northern part, at 30.7°S, which is also compatible with a significant component of southward displacement in that area. These trench-parallel displacements are consistent with a radial, centripetal pattern of horizontal displacement vectors pointing toward the centroid of the earthquake. This effect is most pronounced toward the north and south edges of the main slip area, a feature that can be used to refine source models of the earthquake.

3.2. Comparison with GPS data

Projection of GPS displacements in the line-of-sight and along the direction of the satellite track allows for validating the accuracy of the interferometric products for across-track and along-track interferograms, respectively (Figure 3). This comparison yields a root mean square (RMS) residual of 7.8 cm and 7.0 cm for ascending and descending across-track interferograms, respectively. This residual is close to the fluctuations of 1–2 fringes usually observed within across-track C-band interferograms in north-central Chile [*Ducret*, 2013]. Linear regression between across-track InSAR and GPS projected in the LOS shows an excellent mutual agreement, with a coefficient of correlation above 0.98 and a proportionality factor within 10% of unity.

For the along-track component, the RMS equals 3.5 cm and 5.9 cm for ascending and descending geometries, respectively. This sub-decimetric misfit is in agreement with theoretical expectations (see Appendix A for details). The slope of the linear regression is close to 0.8 in either case. This value departs from unity, which may be due to bias on the slope determination imparted by misfits on the few points located in the area of maximum displacement along the coast. In particular, maximum misfit in the descending along-track interferogram chiefly occurs at site EMAT, which has recorded a peak westward displacement of 220 cm. Due to instrument malfunction, the GPS-derived coseismic displacement at EMAT includes 2 days of post-seismic displacement that are largely absent in the descending interferogram (post-quake image acquired +11 hours after mainshock). Yet, significant post-seismic motion, likely resulting from rapid afterslip, is evident in time-series from cGPS sites located along the coast (6–7 cm eastward displacement is recorded in the 24 hours following the mainshock at sites CMBA and PFRJ). Therefore, significant residual post-seismic motion may explain part of the misfit at EMAT.

3.3. 3D displacement field

The 3D displacement field can be deduced from the four components of ground motion sensed by across- and along-track interferograms on both ascending and descending geometries (Figure 4). This is achieved by solving an overdetermined linear system involving 3 unknowns and 4 equations, consisting in the LOS and azimuth displacements in ascending and descending passes. The agreement between GPS- and InSAR-derived displacements is below 3 cm for the vertical and east-west components, which are best resolved. The RMS is only slightly higher (5.3 cm) for the north-south component, wich would otherwise remain unresolved by standard across-track InSAR. The rotation of displacement vectors along the shoreline is well reproduced, as well as the shift from coastal subsidence to coastal uplift at 31.1°S. This change is consistent with vertical motion recorded by intertidal fauna [*Ruiz et al.*, 2016]. Coseismic slip extending below the continent near the epicenter, and remaining offshore further to the north, explains this feature [*Ruiz et al.*, 2016; *Melgar et al.*, 2016].

4. Conclusion

This study demonstrates the capability of the Sentinel-1 system, operating in wide-swath TOPS mode, to capture the full 3D displacement field of large subduction earthquakes at sub-decimetric accuracy for all three components. In the particular case of an earthquake where horizontal displacement is predominantly east-west, and displacements vary smoothly, such as large subduction earthquakes in South America, Japan or

Cascadia, Sentinel-1 allows for quickly and exhaustively mapping surface displacement. For shallower and/or smaller earthquakes, the method may partly miss the variability of the displacement over length scales smaller than 10 km, as along-track interferometry is only practicable in burst overlap regions. Nevertheless, within burst overlap regions, the along-track component of displacement is available at dense spatial sampling, and is not influenced by tropospheric phase screen. This is similar to having a densely-spaced campaign GPS transect at disposal, which already represents a substantial improvement. Between these sparse burst overlap regions, conventional split-beam and/or offset-tracking can provide a background measurement, albeit with less accuracy [*Jung et al.*, 2014; *Scheiber et al.*, 2015]. Future development of agile SAR antennas and innovative acquisition modes, such as Bi-Directional SAR or SuperSAR, should provide two simultaneous squinted views with continuous spatial sampling [*Mittermayer et al.*, 2013; *Jung et al.*, 2015], thereby truly extending the InSAR technique towards full 3D capability.

Appendix A: Along-track ground displacement from TOPS interferometry

A1. Principle of "burst overlap interferometry"

In along-track double-difference interferograms, the azimuth displacement Δx_{az} is proportional to the azimuth time shift induced by target displacement along the azimuth time axis Δt_{az} (or equally the azimuth misregistration) and to the difference in instantaneous Doppler frequency Δf_{ovl} between forward and backward view in the overlap region [*Scheiber and Moreira*, 2000]:

$$\Delta\Phi_{\mathrm{ovl}} = 2\pi\Delta f_{\mathrm{ovl}}\Delta t_{\mathrm{az}} = 2\pi\Delta f_{\mathrm{ovl}}\frac{\Delta x_{\mathrm{az}}}{\Delta x_{\mathrm{s}}}\Delta t_s \quad \text{(A1)}$$

where Δt_s is the azimuth sampling and Δx_{s} is the azimuth pixel size. In TOPS wide-swath mode, the frequency difference Δf_{ovl} is the product of the effective Doppler rate K_t and the duration of a full TOPS cycle T_{cycle} [*Prats-Iraola et al.*, 2012]:

$$\Delta f_{\mathrm{ovl}} = |K_t| T_{\mathrm{cycle}} \tag{A2}$$

The effective Doppler rate K_t results from the combination of the classical Doppler rate induced by platform motion K_a and the supplemental effect K_s induced by beam steering at a rate k_Ψ from the aft to the fore [*De Zan and Guarnieri*, 2006]:

$$K_t = \frac{K_a K_s}{K_a - K_s} \quad ; \quad K_a = -\frac{2v_s^2}{\lambda R_o} \quad ; \quad K_s \approx \frac{2v_s}{\lambda} k_\Psi \tag{A3}$$

The same result can be deduced equivalently by considering the difference between line-of-sight (LOS) vectors for the two observation directions available in burst overlaps. The azimuth displacement is the projection of ground motion $\vec{u}_{\mathrm{displ}}$ onto the difference, within the overlap region, between the LOS vectors $\vec{k}_{\mathrm{fw}}$ and $\vec{k}_{\mathrm{bw}}$ of the forward interferogram and the backward interferogram, respectively (Figure 1b) :

$$\begin{aligned} \Delta\Phi_{\mathrm{ovl}} = (\Delta\Phi_{\mathrm{fw}} - \Delta\Phi_{\mathrm{bw}}) &= \frac{4\pi}{\lambda} \vec{u}_{\mathrm{displ}} . \left(\vec{k}_{\mathrm{fw}} - \vec{k}_{\mathrm{bw}}\right) \\ &= \frac{4\pi}{\lambda} \Delta x_{\mathrm{az}} \, . \, ||\vec{j}_{\mathrm{diff}}|| \end{aligned} \tag{A4}$$

$$\text{with} \quad : \quad \vec{j}_{\mathrm{diff}} = \vec{k}_{\mathrm{fw}} - \vec{k}_{\mathrm{bw}} \approx \Delta\Psi_{\mathrm{ovl}} \, . \, \vec{j}_{\mathrm{along-track}} \tag{A5}$$

where $\vec{j}_{\mathrm{along-track}}$ is a horizontal unit vector parallel to the satellite track. In TOPS mode, the squint angle difference $\Delta\Psi_{\mathrm{ovl}}$ between two consecutive overlaps for a given sub-swath can be deduced from the beam steering rate k_Ψ and the time separation between overlaps $\Delta\eta_{\mathrm{ovl}}$:

$$\Delta\Psi_{\mathrm{ovl}} = \Delta\eta_{\mathrm{ovl}} k_\Psi \tag{A6}$$

Typical numerical values of the above parameters for Sentinel-1 TOPS IW mode are provided in Table A1. Ultimately, the along-track displacement Δx_{az} (in cm) is obtained by multiplying the double-difference phase $\Delta\Phi_{\mathrm{ovl}}$ (in radian) by a factor $\sim 21 - 25$ cm/rad, meaning that a full along-track fringe represents an along-track displacement of ~ 130 cm (for comparison, the radian-to-cm convertion factor equals ~ 0.44 cm/rad for the ~ 2.8 cm across-track fringe).

A2. Uncertainty assessment

From a signal processing point-of-view, the theoretical accuracy achieved by the double-difference interferogram in burst overlaps is given by the error standard deviation [*Bamler and Eineder*, 2005; *Prats-Iraola et al.*, 2012] :

$$\sigma_{ovl} = \frac{1}{2\pi\Delta f_{\mathrm{ovl}}} \frac{1}{\sqrt{N}} \frac{\sqrt{1-\gamma^2}}{\gamma} \frac{1}{\Delta t_s}, \qquad \text{(A7)}$$

here provided in units of resolution elements. In this expression, N is the number of pixels used in the spatial averaging, γ is the coherence and Δf_{ovl} is the spectral separation in the overlap region (~ 4 kHz for Sentinel IW). As shown in Figure A1, the expected accuracy strongly depends on the number of independent pixels used in the averaging, but less so on the coherence. In case of a uniform shift across the whole burst overlap region (i.e. no deformation), N may exceed a million pixels, so that an accuracy better than 0.1 cm can be reached. However, the accuracy decreases to 0.3–1 cm if displacement changes over distances of the order of 1 km, and up to 10 cm for 100 m posting in adverse coherence conditions. These estimates are in rough agreement with the residual fit to the GPS measured for the Illapel earthquake data set (RMS=3–5 cm, Section 3.2), which corresponds to relatively good coherence conditions ($\gamma > 0.5$). For comparison, the standard deviations from Coherent cross-correlation (CCC) [*Bamler and Eineder*, 2005; *De Zan*, 2011] and Incoherent (amplitude) cross-correlation (ICC) [*De Zan*, 2014] are, respectively :

$$\sigma_{ICC} = \sqrt{\frac{3}{2N}} \frac{\sqrt{1-\gamma^2}}{\pi\gamma} \quad ; \quad \sigma_{CCC} = \sqrt{\frac{3}{10N}} \frac{\sqrt{2+5\gamma^2-7\gamma^4}}{\pi\gamma^2} \tag{A8}$$

For a given number of averaged pixels, the performance of the present method is better, by one order ot magnitude, than that of ICC and CCC (Figure A1).

From a practical point of view, the double-difference along-track phase is not contaminated by atmospheric phase screen, which is the main source of error for multi-temporal InSAR [e.g. *Zebker et al.*, 1997; *Hanssen*, 2001]. Nevertheless, along-track InSAR being a relative measurement, it can be affected by long-spatial-wavelength nuisance stemming from residual large-scale misregistration due to geometric approximations and/or orbit errors. This effect translates locally into a bias that may reach several centimeters. This bias can be mitigated by adjustment of a planar or higher order polynomial trend in distant regions unaffected by the tectonic signal, or accounted for as an unknown during source modeling. Alternatively, external data, such as GPS, can be used to provide a reference. Interpolation between burst overlaps can also lead to aliasing of the displacement field. The induced errors depend on the smallest spatial wavelength of the deformation. In particular, a complex displacement field (e.g. induced by shallow faulting) will significantly jeopardize the validity of the interpolation.

Acknowledgments.

The Sentinel-1 data used for this study are provided by ESA / Copernicus. Interferometric processing was carried out using a modified version of ROI_PAC software [*Rosen et al.*, 2004]. Most figures were designed and some processing steps (filtering, interpolation) were performed with help of GMT software [*Wessel and Smith*, 1991]. The GPS observations used in this study were acquired through the Centro Sismólogico Nacional (CSN) and the French–Chilean Laboratoire International Associé (LIA) geodetic networks. This project was supported by PNTS grant number "PNTS-2015-09" and by the "MEGACHILE" project funded by the Agence Nationale de la Recherche (ANR). This is IPGP contribution number 3721.

References

Bamler, R., and M. Eineder (2005), Accuracy of differential shift estimation by correlation and split-bandwidth interferometry for wideband and delta-k sar systems, *Geoscience and Remote Sensing Letters, IEEE*, *2*(2), 151–155.

Barbot, S., Y. Hamiel, and Y. Fialko (2008), Space geodetic investigation of the coseismic and postseismic deformation due to the 2003 Mw7. 2 Altai earthquake: Implications for the local lithospheric rheology, *Journal of Geophysical Research: Solid Earth (1978–2012)*, *113*(B3).

Bechor, N. B., and H. A. Zebker (2006), Measuring two-dimensional movements using a single InSAR pair, *Geophysical research letters*, *33*(16).

De Zan, F. (2011), Coherent shift estimation for stacks of sar images, *Geoscience and Remote Sensing Letters, IEEE*, *8*(6), 1095–1099.

De Zan, F. (2014), Accuracy of incoherent speckle tracking for circular gaussian signals, *IEEE Geoscience and Remote Sensing Letters*, *11*(1), 264–267.

De Zan, F., and A. M. Guarnieri (2006), TOPSAR: Terrain observation by progressive scans, *Geoscience and Remote Sensing, IEEE Transactions on*, *44*(9), 2352–2360.

De Zan, F., P. Prats-Iraola, R. Scheiber, and A. Rucci (2014), Interferometry with tops: coregistration and azimuth shifts, in *EUSAR 2014; 10th European Conference on Synthetic Aperture Radar; Proceedings of*, pp. 1–4, VDE.

De Zan, F., P. Prats-Iraola, and M. Rodriguez-Cassola (2015), On the dependence of delta-k efficiency on multilooking, *Geoscience and Remote Sensing Letters, IEEE*, *12*(8), 1745–1749.

Ducret, G. (2013), Mesure de déformation par interférométrie radar : développements méthodologiques et applications à la subduction chilienne., Ph.D. thesis, Institut de Physique du Globe de Paris, France.

Fialko, Y., M. Simons, and D. Agnew (2001), The complete (3-D) surface displacement field in the epicentral area of the 1999 M_w7.1 Hector Mine earthquake, California, from space geodetic observations, *Geophys. Res. Lett.*, *28*(16), 3063–3066, doi:10.1029/2001GL013174.

Goldstein, R. M., H. A. Zebker, and C. L. Werner (1988), Satellite radar interferometry-two-dimensional phase unwrapping, *Radio science*, *23*(4), 713–720.

González, P. J., M. Bagnardi, A. J. Hooper, Y. Larsen, P. Marinkovic, S. V. Samsonov, and T. J. Wright (2015), The 2014–2015 eruption of Fogo volcano: Geodetic modeling of Sentinel-1 TOPS interferometry, *Geophysical Research Letters*, *42*(21), 9239–9246.

Grandin, R. (2015), Interferometric Processing of SLC Sentinel-1 TOPS Data, in *Proceedings of the 2015 ESA Fringe workshop, ESA Special Publication, SP*, vol. 731.

Grandin, R., A. Socquet, R. Binet, Y. Klinger, E. Jacques, J.-B. de Chabalier, G. King, C. Lasserre, S. Tait, P. Tapponnier, et al. (2009), September 2005 Manda Hararo-

Dabbahu rifting event, Afar (Ethiopia): constraints provided by geodetic data, *Journal of Geophysical Research: Solid Earth (1978–2012)*, *114*(B8).

Grandin, R., M. Vallée, C. Satriano, R. Lacassin, Y. Klinger, M. Simoes, and L. Bollinger (2015), Rupture process of the mw= 7.9 2015 gorkha earthquake (nepal): insights into himalayan megathrust segmentation, *Geophysical Research Letters*, *42*(20), 8373–8382.

Hanssen, R. F. (2001), *Radar interferometry: data interpretation and error analysis*, vol. 2, Springer Science & Business Media.

Holzner, J., and R. Bamler (2002), Burst-mode and scansar interferometry, *Geoscience and Remote Sensing, IEEE Transactions on*, *40*(9), 1917–1934.

Jung, H.-S., J.-S. Won, and S.-W. Kim (2009), An improvement of the performance of multiple-aperture SAR interferometry (MAI), *Geoscience and Remote Sensing, IEEE Transactions on*, *47*(8), 2859–2869.

Jung, H.-S., W.-J. Lee, and L. Zhang (2014), Theoretical Accuracy of Along-Track Displacement Measurements from Multiple-Aperture Interferometry (MAI), *Sensors*, *14*(9), 17,703–17,724.

Jung, H.-S., Z. Lu, A. Shepherd, and T. Wright (2015), Simulation of the supersar multi-azimuth synthetic aperture radar imaging system for precise measurement of three-dimensional earth surface displacement, *Geoscience and Remote Sensing, IEEE Transactions on*, *53*(11), 6196–6206.

Melgar, D., W. Fan, S. Riquelme, J. Geng, L. Liang, M. Fuentes, G. Vargas, R. Allen, P. Shearer, and E. Fielding (2016), Slip segmentation and slow rupture to the trench during the 2015, Mw8.3 Illapel, Chile earthquake, *Geophys. Res. Lett.*

Meta, A., P. Prats, U. Steinbrecher, J. Mittermayer, and R. Scheiber (2008), TerraSAR-X TOPSAR and ScanSAR comparison, in *Synthetic Aperture Radar (EUSAR), 2008 7th European Conference on*, pp. 1–4, VDE.

Michel, R., J.-P. Avouac, and J. Taboury (1999), Measuring ground displacements from SAR amplitude images: application to the landers earthquake, *Geophys. Res. Lett.*, *26*, 875–878, doi:10.1029/1999GL900138.

Mittermayer, J., S. Wollstadt, P. Prats-Iraola, P. López-Dekker, G. Krieger, and A. Moreira (2013), Bidirectional sar imaging mode, *Geoscience and Remote Sensing, IEEE Transactions on*, *51*(1), 601–614.

Peltzer, G., F. Crampé, and G. King (1999), Evidence of nonlinear elasticity of the crust from the Mw7. 6 Manyi (Tibet) earthquake, *Science*, *286*(5438), 272–276.

Prats-Iraola, P., R. Scheiber, L. Marotti, S. Wollstadt, and A. Reigber (2012), TOPS interferometry with TerraSAR-X, *Geoscience and Remote Sensing, IEEE Transactions on*, *50*(8), 3179–3188.

Pritchard, M., C. Ji, and M. Simons (2006), Distribution of slip from 11 mw¿ 6 earthquakes in the northern chile subduction zone, *Journal of Geophysical Research: Solid Earth (1978–2012)*, *111*(B10).

Rosen, P. A., S. Henley, G. Peltzer, and M. Simons (2004), Updated Repeat Orbit Interferometry Package Released, *Eos Trans. AGU*, *85*(5), 47–47, doi:10.1029/2004EO050004.

Ruiz, S., E. Klein, E. Rivera, P. Poli, M. Métois, C. Vigny, J. C. Baez, G. Vargas, F. Leyton, R. Madariaga, and L. Fleitout (2016), The seismic sequence of the 16 September 2005, Illapel Mw 8.3 earthquake, *Seismological Research Letters, under review.*

Scheiber, R., and A. Moreira (2000), Coregistration of interferometric sar images using spectral diversity, *Geoscience and Remote Sensing, IEEE Transactions on*, *38*(5), 2179–2191.

Scheiber, R., M. Jager, P. Prats-Iraola, F. De Zan, and D. Geudtner (2015), Speckle Tracking and Interferometric Processing of TerraSAR-X TOPS Data for Mapping Nonstationary Scenarios, *Selected Topics in Applied Earth Observations and Remote Sensing, IEEE Journal of*, *8*(4), 1709–1720.

Simons, M., and P. Rosen (2007), Interferometric synthetic aperture radar geodesy, *Treatise on Geophysics*, *3*, 391–446.

Torres, R., P. Snoeij, D. Geudtner, D. Bibby, M. Davidson, E. Attema, P. Potin, B. Rommen, N. Floury, M. Brown, et al. (2012), Gmes sentinel-1 mission, *Remote Sensing of Environment*, *120*, 9–24.

Wessel, P., and W. H. F. Smith (1991), Free software helps map and display data, *EOS Transactions*, *72*, 441–441, doi:10.1029/90EO00319.

Wright, T. J., B. E. Parsons, and Z. Lu (2004), Toward mapping surface deformation in three dimensions using InSAR, *Geophys. Res. Lett.*, *31*(1), 1607, doi:10.1029/2003GL018827.

Zebker, H. A., P. A. Rosen, and S. Hensley (1997), Atmospheric effects in interferometric synthetic aperture radar surface deformation and topographic maps, *Journal of Geophysical Research: Solid Earth (1978–2012)*, *102*(B4), 7547–7563.

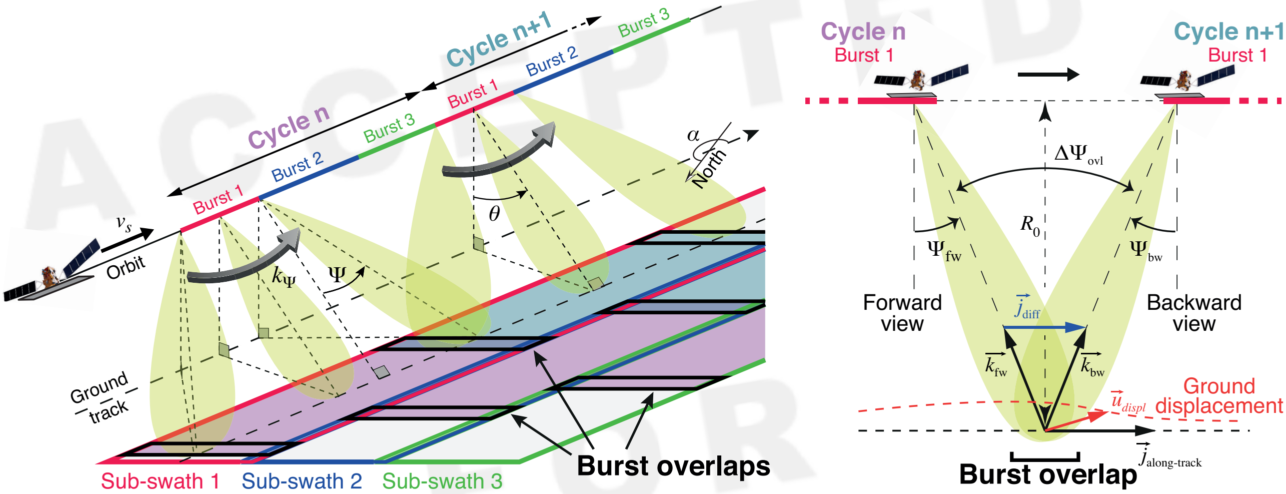

Figure 1. Left: principle of TOPS imaging mode. Right: squint angle diversity in burst overlap regions.

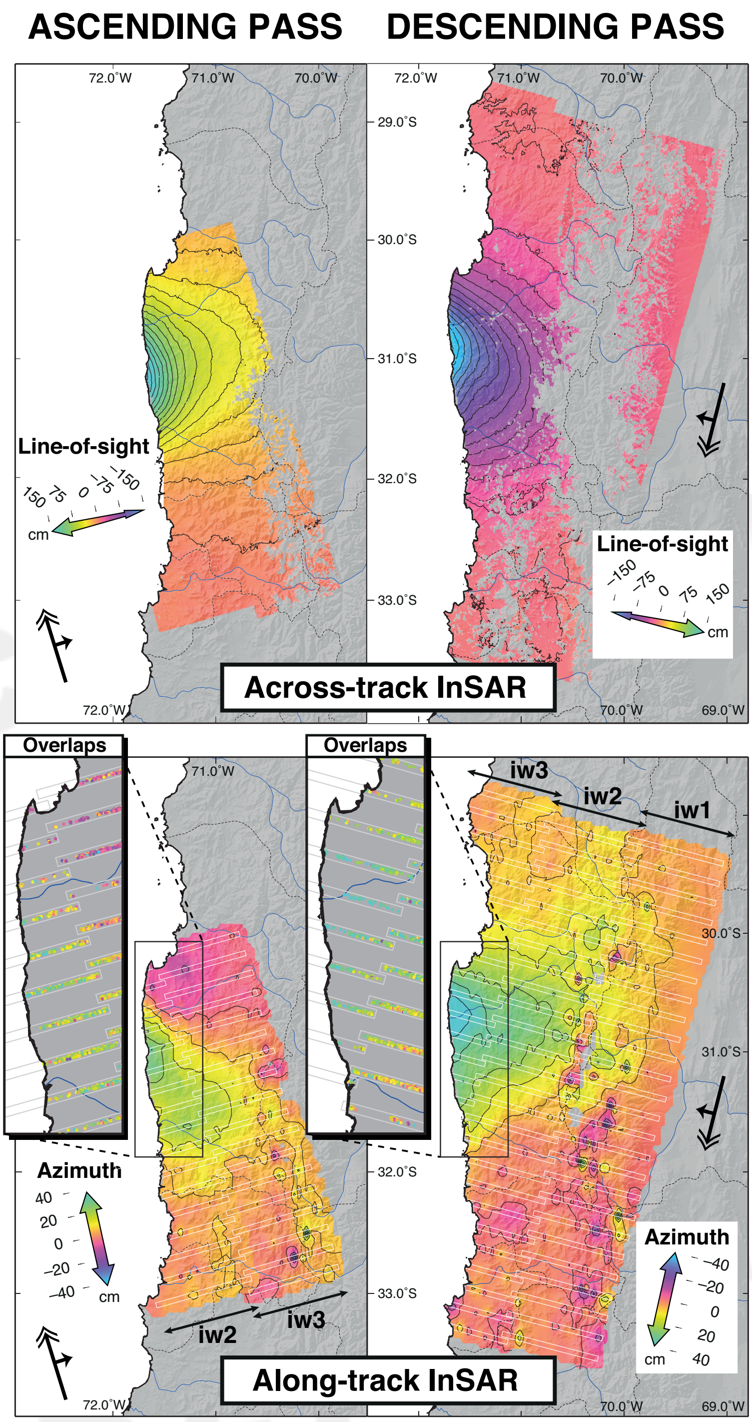

Figure 2. Across-track (top) and along-track (bottom) displacement field from Sentinel-1 InSAR. Note the different color scaling for across-track and along-track InSAR. The left and right panels correspond to ascending and descending passes, respectively. Double headed arrow shows direction of flight of the platform. White rectangles in bottom panels indicate regions of burst overlaps. The along-track displacement field was filtered and interpolated between regions of burst overlaps to produce a continous displacement field. Insets show unfiltered double-difference phase prior to interpolation.

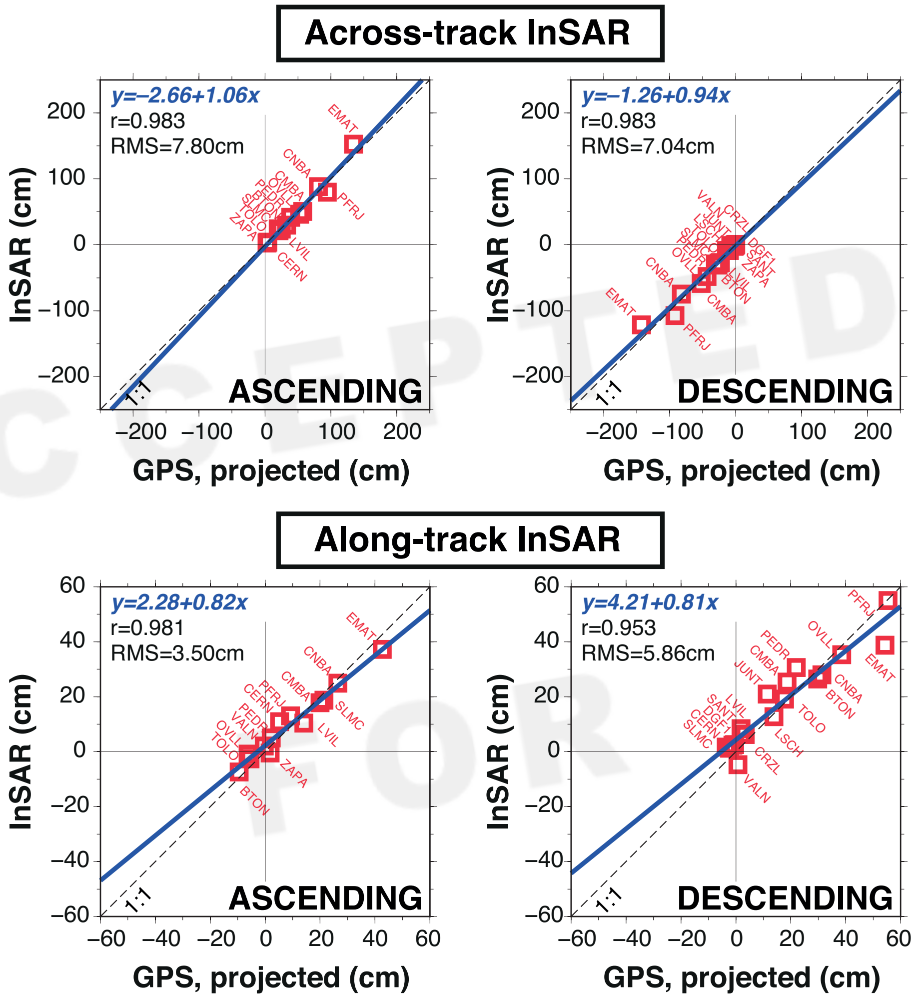

Figure 3. Linear regression between GPS and (top) across-track InSAR or (bottom) along-track InSAR. Left panels are for the ascending pass, right panels for the descending pass (same ordering as in Figure 2). Note the different scaling for across-track and along-track InSAR.

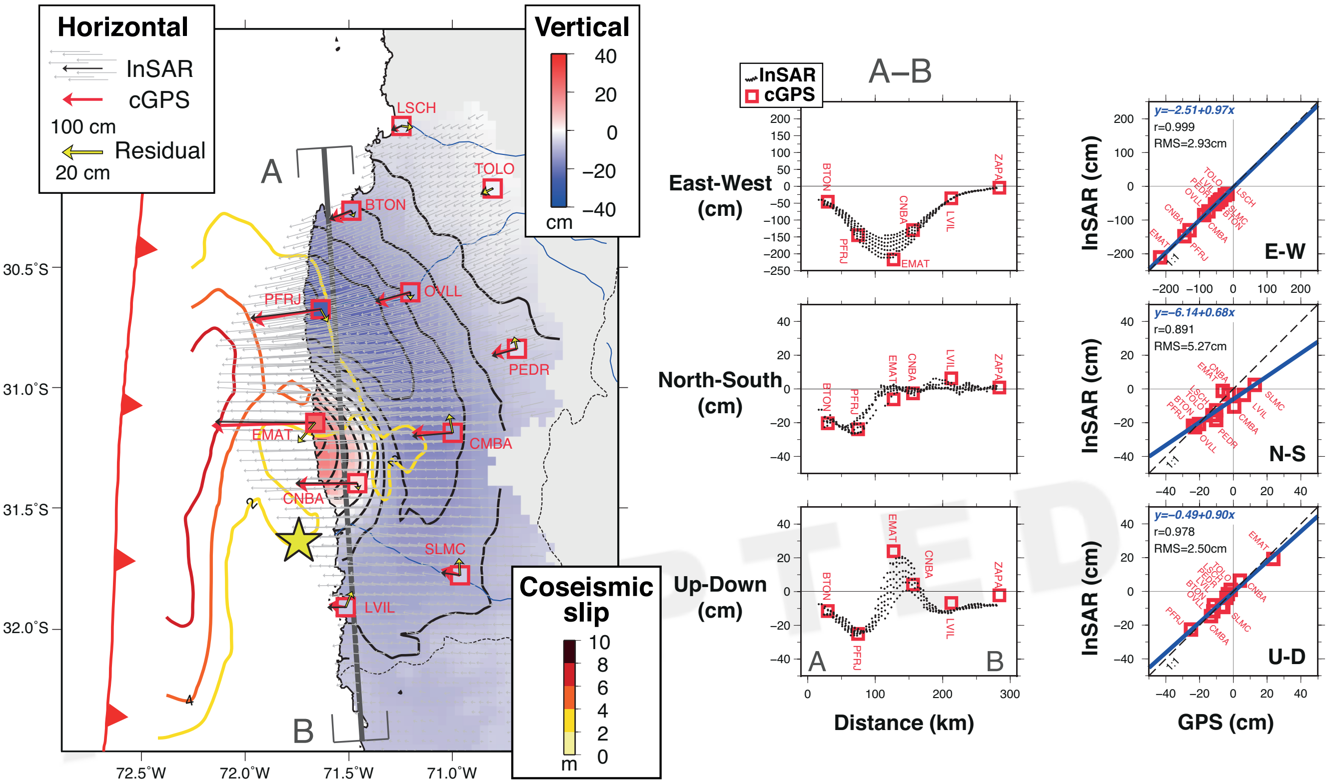

Figure 4. Left: 3D surface displacement reconstructed from Sentinel-1 InSAR. Red arrows show displacement at continous GPS sites (cGPS), while color fill in red squares interior represents the vertical component of displacement from GPS [*Ruiz et al.*, 2016]. Black arrows show displacement deduced from Sentinel-1 InSAR at locations of GPS benchmarks. Residuals are shown in yellow, with enhanced scaling. Grey arrows show horizontal displacement sampled on a regular grid. The colored grid in the background shows the vertical component of displacement on the same regular grid, with contours at 5 cm interval overlaid. Coseismic slip contours from USGS are shown for comparison (http://earthquake.usgs.gov/earthquakes/eventpage/us20003k7a#scientific_finitefault). Center: transect showing comparison between Sentinel-1 InSAR and GPS. Location of the profile is shown in left panel. Top row: east-west component; middle row: north-south component; bottom row: vertical component. Sign convention is right-handed ENU. Note the different scaling for the east-west component. Right: linear regression between Sentinel-1 InSAR and GPS displacements at GPS sites.

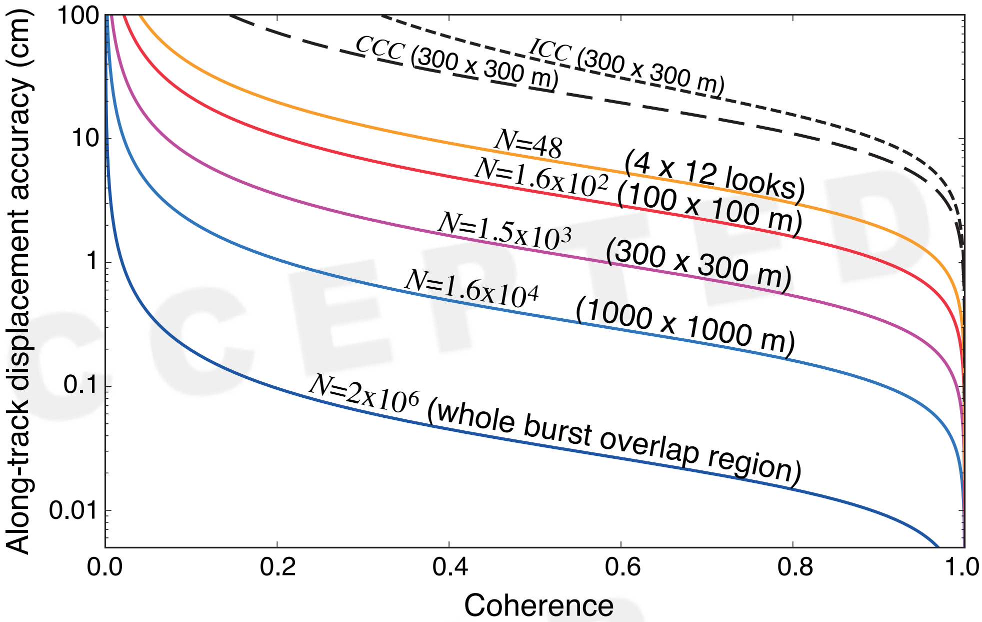

Figure A1. Theoretical accuracy of the along-track displacement achieved by Sentinel-1 burst-overlap interferometry, as a function of coherence γ, for an azimuth pixel size Δx_s =14 m (color lines, Equation A7). Several cases are distinguished, depending on the number of full-resolution pixels N used for the averaging. The accuracy of coherent and incoherent cross-correlation techiques (respectively CCC and ICC) at 300 $\times$ 300 m posting is shown for comparison (black dashed lines, Equation A8).

Table A1. Parameters of Sentinel-1 IW data used in this study (descending pair)

ine ine Sub-swath		1	2	3
ine Range[a]	R_o	829 km	879 km	933 km
Incidence angle[a]	θ	34°	39°	44°
Antenna steering rate	k_Ψ	1.59 deg.s^{-1}	0.98 deg.s^{-1}	1.40 deg.s^{-1}
Time separation between overlaps	$\Delta\eta_{\mathrm{ovl}}$	0.80 s	0.96 s	0.82 s
Squint difference in overlap region	$\Delta\Psi_{\mathrm{ovl}}$	1.28°	0.94°	1.15°
Doppler rate due to platform motion[a]	K_a	−2260 Hz	−2131 Hz	−2008 Hz
Doppler rate due to antenna steering[a]	K_s	7593 Hz	4679 Hz	6672 Hz
Doppler rate in focused SLC[a]	K_t	1742 Hz	1464 Hz	1544 Hz
ine ine Wavelength	λ		5.55 cm	
Platform heading (clockwise w.r.t. north)	α		-167.2°	
Platform velocity	v_S		7211 m.s^{-1}	
Azimuth sampling	Δt_s		0.002056 s	
Azimuth pixel size	Δx_{s}		14.07 m	
Burst cycle duration	T_{cycle}		2.75 s	

[a] At mid-range